Solar Energy Materials & Solar Cells 292 (2025) 113821

Contents lists available at ScienceDirect

Solar Energy Materials and Solar Cells

journal homepage: www.elsevier.com/locate/solmat

High efficiency perovskite solar cells with synchronous optimization by formic acid vapor annealing process and composite electron transport layer

Haotian Zhang [a,b,c], Chao Gao [a,b,c], Li He [a,b,c], Dezhao Zhang [a,b,c], Hongzhen Su [a,b,c], Hong Liu [a,b,c], Kadi Zhu [c,*], Wenzhong Shen [a,b,c,d,**]

[a] Institute of Solar Energy, And Key Laboratory of Artificial Structures and Quantum Control (Ministry of Education), School of Physics and Astronomy, Shanghai Jiao Tong University, Shanghai, 200240, People's Republic of China
[b] Shanghai Non-carbon Energy Conversion and Utilization Institute, Shanghai, 200240, People's Republic of China
[c] School of Physics and Astronomy, Shanghai Jiao Tong University, Shanghai, 200240, People's Republic of China
[d] Collaborative Innovation Center of Advanced Microstructures, Nanjing, 210093, People's Republic of China

ARTICLE INFO

Keywords:
Perovskite solar cells
HCOOH
Vapor annealing method
Grain size
Defect passivation
Energy level alignment
Interfacial modification
Deprotonation reaction

ABSTRACT

The thermal annealing process is significant for the crystallization of perovskite films ($(FAPbI_3)_{0.9}(MAPbBr_3)_{0.1}$). However, conventional annealing methods suffer from non-uniform heating of film samples. Herein, we report a vapor annealing method that the perovskite film was annealed in formic acid vapor, generating a uniform thermal field to control crystallization. Simultaneously, HCOOH efficiently enhances sample crystallinity, passivates defects and suppresses deprotonation, establishing an optimal physicochemical environment for perovskite growth. In addition, the electron transport layer (ETL) composed of SnO_2 and ZnO nanoparticles (NPs) demonstrates enhanced electrical conductivity and light transmittance. Methylammonium Chloride (MACl) is introduced to suppress ZnO NPs-induced deprotonation. The experimental and theoretical results manifest the mechanism of inhibiting the deprotonation reaction by MACl. The stable power conversion efficiency (PCE) of the device prepared by this method achieves 23.41 % and maintains 83 % of initial PCE during the long-term stability test.

1. Introduction

Owing to the demand for next-generation optoelectronic materials, perovskite have garnered significant attention due to its low cost, low energy consumption, high absorption coefficient, and flexible fabrication [1–5]. Organic-inorganic halide perovskite solar cells (PSCs) can be applied in scenarios where conventional crystalline silicon (c-Si) solar cells are not competent for excellent performance in low light illumination condition and adjustable transparency [6–9]. Within a decade of research, the PCE of PSCs have reached 26.81 %, which is very close to the record of c-Si solar cells [10]. However, the current PCE remains significantly below the 33.7 % theoretical limit predicted by the Shockley-Queisser (S-Q) theory [11]. The device stability and photon absorption utilization efficiency require further optimization. In order to further improve the PCE of the device, it is necessary to optimize the crystallization of the perovskite film and develop more practical interface modification strategies.

The annealing process is pivotal for modulating perovskite crystallization dynamics and film quality. Various strategies have been developed to optimize annealing, including studies on temperature-dependent morphology evolution in perovskite films [12,13]. Elevating the annealing temperature or extending the annealing time can improve film crystallinity by promoting crystal growth and facilitating recrystallization. [14,15]. However, conventional annealing relies on bottom-up heating, leading to inhomogeneous temperature distribution within perovskite films [16]. Such thermal gradients cause asynchronous crystallization: Lewis acid-base reactions initiate at low temperatures, resulting in non-uniform grain sizes, disordered crystal orientations, and degraded crystallinity [17]. Maintaining uniform film temperature during annealing is critical to ensure consistent Lewis acid-base reactions and nucleation rates across the film, forming stable growth interfaces, reducing crystallization energy barriers, and

* Corresponding author.
** Corresponding author. Institute of Solar Energy, and Key Laboratory of Artificial Structures and Quantum Control (Ministry of Education), School of Physics and Astronomy, Shanghai Jiao Tong University, Shanghai, 200240, People's Republic of China.
E-mail addresses: zht123@sjtu.edu.cn (H. Zhang), wzshen@sjtu.edu.cn (W. Shen).

https://doi.org/10.1016/j.solmat.2025.113821
Received 14 April 2025; Received in revised form 11 June 2025; Accepted 30 June 2025
Available online 3 July 2025

increasing grain size [18–24]. Moreover, the sensitivity of precursors to residual moisture and solvents leads to batch-to-batch variations, which result from slight fluctuations in processing conditions and highlight the climate-dependent nature of perovskite fabrication [25,26]. Developing new annealing methods with uniform thermal fields and stable environments is essential for reproducible perovskite crystallization. Li et al. demonstrated liquid medium annealing is an effective approach to regulate halide perovskite crystal growth, where a constant liquid heating field yielded films with high crystallinity, fewer defects, and improved homogeneity [24]. Wang and co-workers employed a perfluorinated toluene solvent bath annealing method to enhance perovskite film quality and fabricate high-performance PSCs [27]. However, residual liquid media may negatively impact photovoltaic performance, and fabrication costs remain high. Liu et al. investigated solvent vapor annealing, which influenced film growth and morphology, but efficiencies via direct antisolvent vaporization were suboptimal [28]. Developing a more tunable, low-cost, and homogeneous annealing process is critical for improving perovskite film crystallinity.

Herein, we employ a method to optimize perovskite films via annealing in a HCOOH vapor environment. HCOOH vapor annealing ensures uniform film heating, mitigating crystallinity inconsistencies caused by thermal gradients and enhancing overall film quality. The vapor environment also offers superior tunability and stability. The reducing properties of HCOOH passivate defect states, inhibit oxidation, reduce trap-state density, enhance charge carrier mobility, and improve device stability. Concurrently, HCOOH vapor provides an ideal physicochemical environment for perovskite crystal growth. Additionally, the electron transport layer (ETL) [29–32] is optimized using ZnO NPs to improve the electrical conductivity and light transmittance of SnO_2--based ETLs. This modification enhances energy level alignment and charge transport within the device. Meanwhile, MACl in the perovskite layer effectively suppresses ZnO-induced deprotonation. Finally, the optimized device achieves a stable PCE of 23.41 % and retains 83 % of its initial efficiency after 3000 h of stability testing.

2. Result and discussion

In contrast to the traditional annealing process on the hot-plate demonstrated in Fig. 1a (top), we used the vapor medium annealing process shown in Fig. 1a (bottom) to fabricate perovskite films in preheated HCOOH vapor medium. Different from the bottom-up heating mode on the hot-plate, vapor medium annealing process provides a more uniform heating environment to regulate the crystal growth where the hot steam heats the perovskite film from all directions. The finite element analysis method performed by Comsol Multiphysics software was used to simulate the annealing process in Fig. 1b, which illustrates that vapor medium annealing process provides a faster heating rate. The control perovskite film annealed by traditional annealing process required ~8 s to reach 100 °C, leading to the retarded heating at the surface of perovskite film while directional crystallization had already commenced [33]. In contrast, vapor medium annealing reached 100 °C in just 3.2 s due to the immediate and uniform contact between the hot steam and the entire perovskite film. Fig. S1 shows the simulated heating rate curves for the perovskite film surface, confirming that vapor medium annealing provides faster heating rates and more favorable conditions for perovskite growth. Besides optimizing the physical environment of heating field to modulate the crystalline dynamics during annealing process, HCOOH also provides a powerful chemical environment for passivating the defect in perovskite. HCOOH can inhibit the negative reactions in traditional organic-inorganic halide perovskite materials effectively. As shown in Fig. S2, HCOOH eliminates undesirable iodide oxidation of I^- in the perovskite film due to the reductive effect of $HCOO^-$, as described in Eqs. 1, 2, 5 and 6. The H^+ generated by the reaction and the H^+ in HCOOH simultaneously inhibit

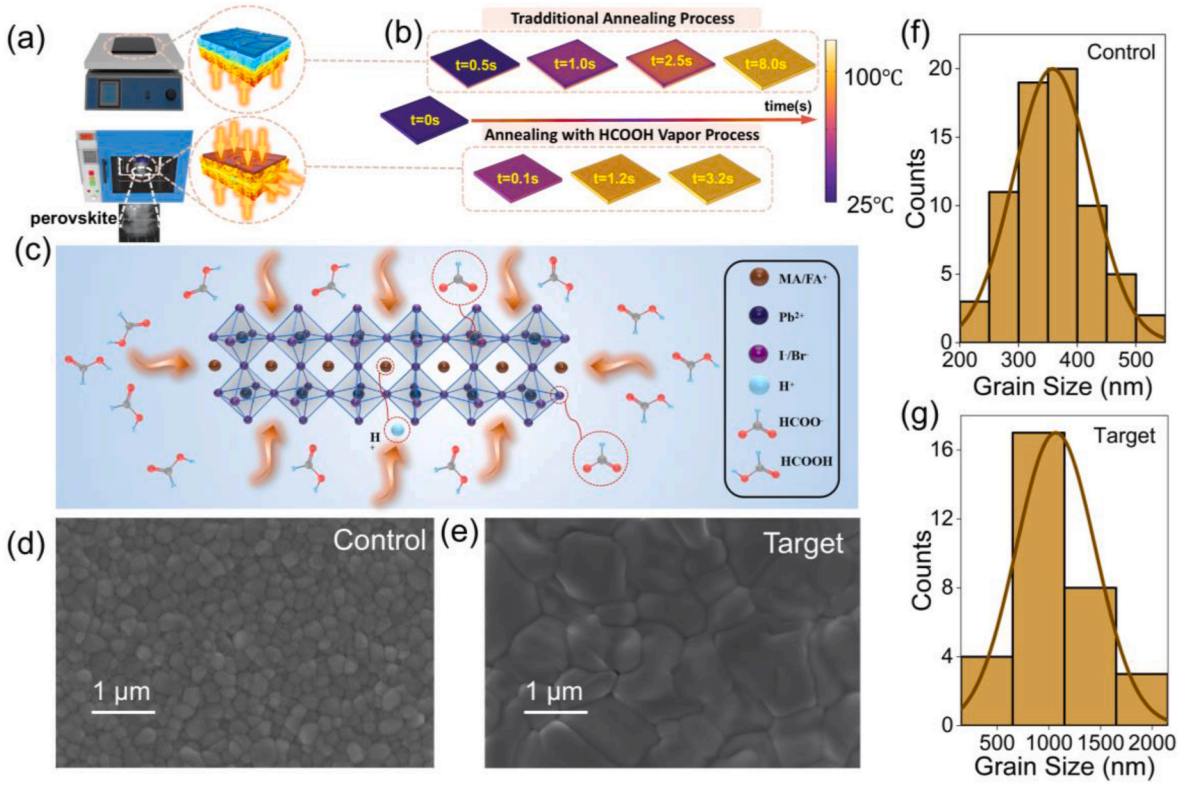

Fig. 1. a) The schematic diagram of traditional annealing process (top), vapor medium annealing process (bottom) and corresponding heating mode. The perovskite of the vapor medium annealing method is located at the bottom of the container, which is indicated by the white dotted circle in the lower figure. b) Simulation results for traditional and vapor medium annealing process by Comsol software. c) The schematic diagram detailed growth dynamics using the vapor medium annealing process. Top-view SEM images d) control film and e) target film. The grain sizes statistics of f) control film and g) target film.

the deprotonation of MA^+ and FA^+, as shown in Eqs. 3, 4, 7 and 8 [33]. We demonstrate successful growth of highly crystalline perovskite films using HCOOH vapor medium annealing. We found that direct spin-coating of HCOOH on the perovskite surface caused no obvious changes in morphology (Fig. S3). Then we modulate the parameters including temperature and the content of HCOOH during the annealing process and observe the morphologies of corresponding samples demonstrated in top-view scanning electron microscope (SEM) images of Figure S4 and Figure S5, where the 10 mmol L^{-1} HCOOH concentration and 100 °C are the best conditions of the vapor medium annealing process. Inappropriate concentration or temperature conditions may result in poor crystallinity of the film. The SEM images and the grain sizes statistics of perovskite treated by traditional annealing process and vapor medium process are shown in Fig. 1d, e, 1f and 1g, which illustrate that the film treated by vapor medium annealing process exhibited increased grain size (~1 μm), which is larger than the film produced by traditional annealing process (350 nm). Since grain boundaries exhibit distinct optoelectronic properties compared to grain interiors, the increased grain size achieved through vapor medium annealing reduces grain boundary density and improves optoelectronic uniformity [34]. Perovskite films with large grain size are usually obtained in high temperature condition, where the growth process of grain is overwhelmed by facilitating the reactant diffusion [15]. Therefore, the observed grain enlargement likely results from the rapid heating in the vapor medium, which can minimize the exposure of precursor at low temperatures to the greatest extent. In summary, the HCOOH vapor medium provides a spatially uniform physical heating field and chemical environment compared with traditional annealing process resulting in perovskite polycrystalline films with fewer defects.

To further investigate the properties of perovskite film treated by the vapor medium annealing process (target), we fabricated the perovskite film through the traditional annealing method (control). X-ray diffraction (XRD) experiment was applied on the control and target samples to confirm the crystalline of the films in Fig. 2a. Compared to the control sample (FWHM = 0.21°), the target sample showed narrower XRD peak widths (FWHM = 0.11°), confirming improved crystallinity that complements the larger grain sizes observed by SEM. The result could be attributed to the better physical and chemical environment provided by the HCOOH vapor medium. Furthermore, the time-of-flight secondary ion mass spectroscopy (TOF-SIMS) was conducted to investigate the vertical elements distribution of the films in Fig. 2b and c. Argon Gas Cluster Ion Beam (Ar-GCIB) was used for sputtering the film to prevent introducing other ions that interfere with the measurement result. TOF-SIMS revealed $HCOO^-$ incorporation into the perovskite lattice, suppressing both iodide oxidation and organic cation deprotonation (MA^+/FA^+), thereby enhancing film stability and reducing defects. In addition, 3D distribution of $HCOO^-$ elements was displayed in Fig. S6. Atomic force microscopy (AFM) was used to further understand surface roughness of the films, which demonstrated that the root mean square (RMS) roughness of the control sample is 38.85 nm and the RMS roughness of the target sample is 56.09 nm. The reduced roughness illustrates the uniform crystallization and is more advantageous for device preparation. Larger grain sizes were also observed in the target sample, which were consistent to the previous SEM results. Moreover, the Kelvin probe force microscopy (KPFM) results of the same position as the AFM images show that the surface electronic chemical potential (ECP) of the target sample is significantly higher than the control sample. The target sample also exhibited more homogeneous electrical properties, suggesting improved vertical charge transport in devices.

Previous characterizations revealed superior crystallinity in the vapor-annealed samples and demonstrated the advantages of the HCOOH vapor annealing process. T To study the promotion of the light absorption properties, the ultraviolet–visible (UV–vis) spectral was applied on the corresponding samples. Fig. 3a shows that the target sample exhibits higher absorbance than the control sample. Tauc plot method was used to fit the absorbance spectra to extract bandgaps of 1.57 eV for the control and target samples, which illustrates that the different annealing method has nearly no effect on the bandgap. It demonstrates that the vapor annealing method only optimizes the annealing environment without changing the structure and composition of perovskite. The photoluminescence (PL) spectral was also used to confirm the change of characteristics of luminescence in Fig. 3b. The result shows that the target sample has higher PL intensity than the control sample. PL mapping revealed spatially uniform emission enhancement, consistent with the spectral measurements (Fig. 3d–f). The better absorption and luminescence properties could be attributed to the better crystalline of the target film treated by the vapor annealing process. In addition, the lifetime of the carriers was identified by the time-resolved PL (TRPL) spectral measurements for glass/control film and glass/target film, which prove that the target film has longer lifetime of carriers. It could be explained that nonradiative recombination has been obviously suppressed in the target sample because of fewer defects. To further identify the role of formic acid in perovskite film, the Fourier transform infrared (FTIR) spectroscopy was used to investigate

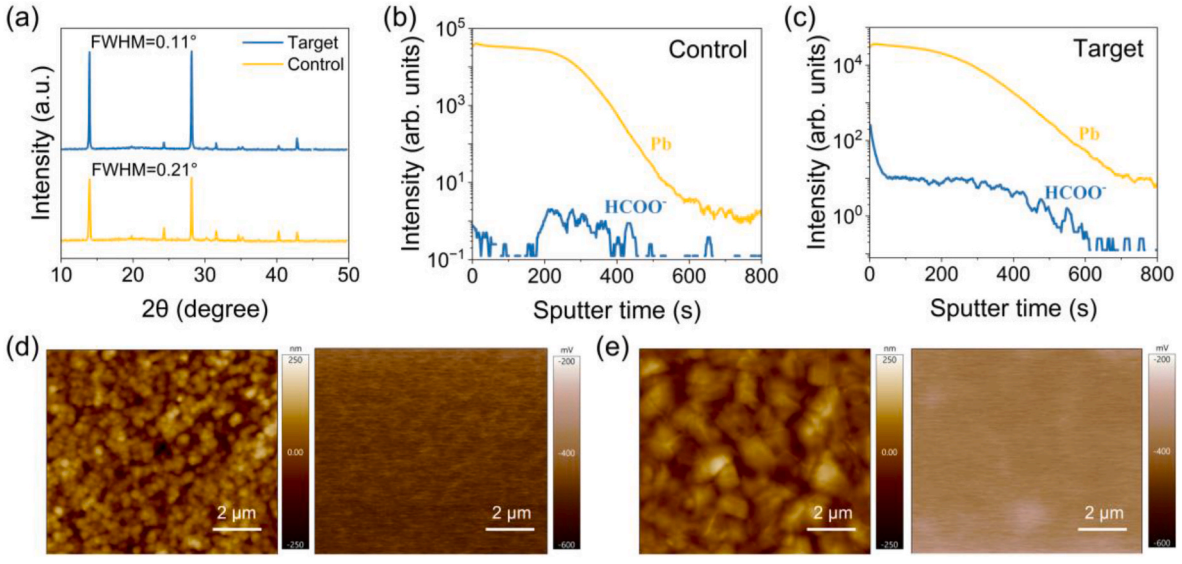

Fig. 2. a) The XRD pattern of control and target samples. TOF-SIMS depth profiles of elements distribution of b) control sample and c) target sample. AFM and FPFM image for d) control sample and e) target sample.

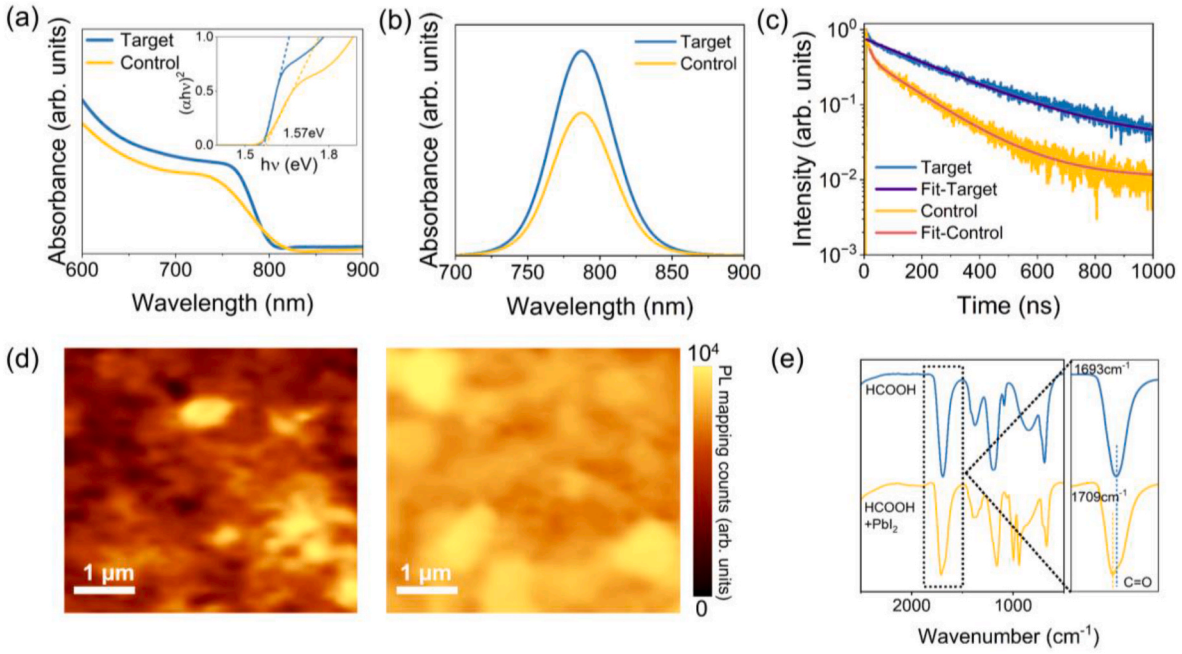

Fig. 3. a) UV–vis absorption spectra of the control/target samples and the fitting results of bandgaps (inner). b) The PL measurements of the PL spectra of glass/control film and glass/target film. c) TRPL spectral of the glass/control film and glass/target film. d) PL mappings of the control sample (left) and target sample (right). e) FTIR spectra of the of pure HCOOH and HCOOH + PbI_2 complex in DMSO.

the interaction of HCOOH and perovskite, the C═O deformation shifts towards higher wavenumbers due to existed interaction. This coordination bonding passivates Pb vacancies, effectively reducing defect density in the perovskite lattice. The sample fabricated by the vapor annealing method exhibits better light absorption and luminescence properties due to the fewer defects and optimized crystalline.

To enhance device performance, we introduced ZnO nanoparticles (NPs) into the ETL film. This modification primarily improved light transmission and electrical conductivity of the film. Fig. 4a shows the energy dispersive spectroscopy (EDS) mapping of SnO_2 and SnO_2: ZnO NPs films, which demonstrate that the existence of Zn element in SnO_2: ZnO NPs sample and ZnO nanoparticles are dissolved in isopropyl alcohol (IPA) with a volume ratio of 1:10. Subsequently, the AFM was used to probe the morphology of the SnO_2 and SnO_2: ZnO NPs films, where the ZnO NPs could be observed clearly in Fig. 4b. 3D AFM images show increased surface roughness due to ZnO NPs incorporation (Fig. S7). The increase of roughness will lead to multiple scattering of light at the rough interface formed by ZnO nanoparticles and SnO_2. Compared to the prior flat surface, incident light undergoes diffuse reflection and scattering at the rough interface between the perovskite

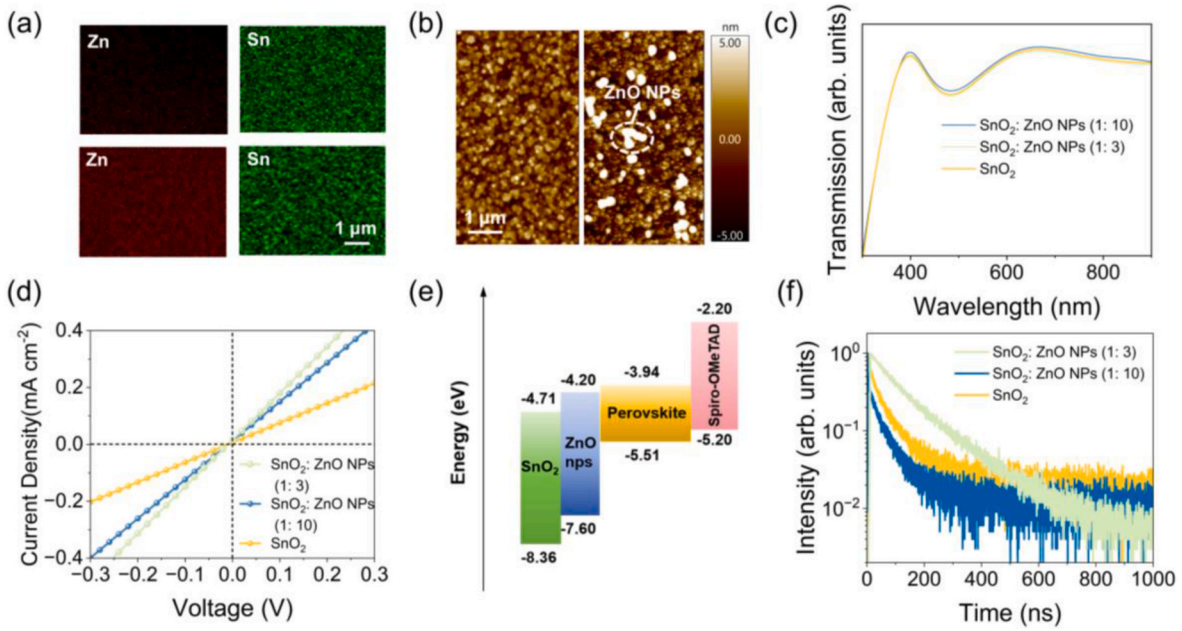

Fig. 4. a) EDS mapping of Zn, Sn elements of SnO_2 (top) and SnO_2: ZnO NPs (bottom) ETL. b) The AFM images of SnO_2 (left) and SnO_2: ZnO NPs (1: 10) (right) ETLs. c) Transmittance spectra of SnO_2 and SnO_2: ZnO NPs films. d) *J-V* curves of ITO/SnO_2 or SnO_2: ZnO NPs/Ag devices. e) Energy level alignment of SnO_2: ZnO NPs ETL. f) TRPL spectral of the ITO/SnO_2/target film and ITO/SnO_2: ZnO NPs/target film devices.

layer and the electron transport layer. This phenomenon prolongs the propagation path of light within the active layer and mitigates specular reflection losses inherent in the previous flat surface configuration, thereby enhancing the effective light transmittance. Optimal roughness randomizes reflection angles, minimizing specular reflection losses. However, excessive NPs loading causes aggregation, leading to nonuniform light scattering and potential perovskite film defects during deposition. In order to explore the appropriate concentration, the morphology of ETL spin-coated by different concentrations of ZnO NPs dissolved in IPA are shown in Fig. S8 and the corresponding devices performance are listed in Table S1, which illustrates that the SnO_2: ZnO NPs (1: 10) ETL exhibits the best performance. The transmission measurement in Fig. 3c was used to demonstrate that the light transmittance performance was promoted by the appropriate concentration ZnO NPs because of the interface optimization and quality improvement of the film. The increase of light transmittance can increase the efficiency of photon utilization of the light absorbing layer, improving the performance of the PSCs. However, excessive concentration of ZnO would cause the decrease in transmittance, which explained the variation tendency of short-circuit current (J_{SC}) in Table S1. Through the current-voltage (*J-V*) test in Fig. 4d applied on the ITO/SnO_2 or SnO_2:ZnO NPs/Ag architecture, a larger slope observed in SnO_2:ZnO NPs film indicated that the conductivity of the ETL was improved by ZnO NPs apparently, which represented better carrier transport ability of ETL with ZnO NPs. It can be attributed to the high electron mobility properties of ZnO (100–200 cm^2V^{-1} s^{-1}), which is significantly better than SnO_2 (10–20 cm^2V^{-1} s^{-1}) [35,36]. Moreover, the introduction of appropriate concentration of ZnO NPs optimizes the energy level alignment in Fig. 4e, which is beneficial to the carrier transformation in different layers in devices and promotes the open circuit voltage (V_{OC}). To verify the promotion of transport ability in ETL, the TRPL measurement was conducted on the ITO/SnO_2/target film and ITO/SnO_2:ZnO NPs (1:10 and 1:3)/target film, respectively. The faster decay in SnO_2:ZnO NPs (1: 10) ETL implies a stronger carrier extraction capability, which could be attributed to the suppressed charge recombination, higher carrier collection efficiency and lower resistance dissipation. But in SnO_2: ZnO NPs (1: 3) ETL, TRPL illustrates that the carrier extraction capability is suppressed due to too thick ZnO layer, which demonstrates the performances of devices fabricated by SnO_2: ZnO NPs (1: 3 and 1: 5) ETLs are significantly degenerated in Table S1.

To further elucidate the superiority of vapor annealing method and SnO_2: ZnO NPs composite ETL, n-i-p planar PSCs with a configuration of ITO/SnO_2: ZnO NPs/target perovskite film/Spiro-OMeTAD/Ag (target device) and ITO/SnO_2/control perovskite film/Spiro-OMeTAD/Ag (control device) were fabricated to investigate their photovoltaic performance, where SnO_2:ZnO NPs/perovskite/Spiro-OMeTAD were prepared by spin-coating method and Ag was prepared by vacuum coating process. The cross-section SEM image of control and target sample PSCs are displayed in Figure S9 and Fig. 5a, which indicate that the larger grain size and smoother surface can be observed in the target sample. The current-voltage (*J-V*) measurement (Fig. 5b) also shows that target sample exhibits a PCE of 23.41 % with an enhanced V_{OC} of 1.19 V, a J_{SC} of 24.38 mA cm^{-2}, and *FF* of 80.70 %, which is obviously promoted from the device fabricated by control sample with a PCE of 19.85 %, V_{OC} of 1.11 V, a J_{SC} of 23.16 mA cm^{-2}, and *FF* of 77.20 %. The PCE, V_{OC} and J_{SC} of PSCs were apparently improved by vapor annealing method, which is consistent with the external quantum efficiency (EQE) measurements of corresponding devices in Fig. 5c. The EQE measurements demonstrated

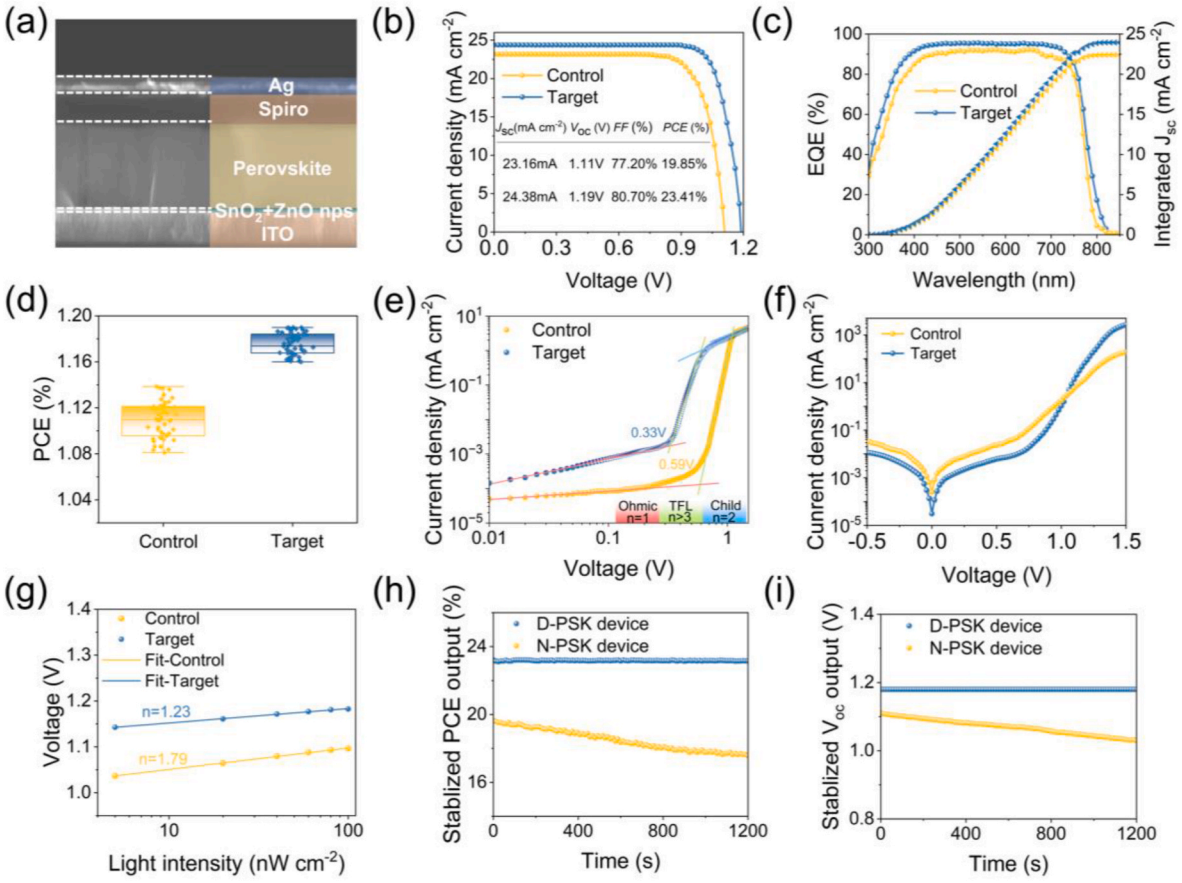

Fig. 5. a) The Cross-section SEM image of target sample PSCs. b) *J-V* measurements of control/target sample PSCs. c) EQE and integrated J_{SC} of the corresponding devices. d) Statistical distribution of PCEs of corresponding devices. e) *SCLC* result of electron-only different devices. f) Dark *J-V* measurements of control/target sample PSCs. g) Dependence of V_{OC} on light intensity. h) PCE and i) V_{oc} measurement under continuous illumination of devices.

that the target sample device exhibits outstanding photo-response and higher integrated current density. The optimized photovoltaic parameters of target device could be ascribed to excellent crystallinity in target perovskite films and enhanced photoelectric properties promoted by ZnO NPs in ETL. Moreover, statistical analyses of 50 individual PSCs made by different annealing methods were summarized in Fig. 5d and Fig. S10. To further investigate the internal charge transport process, the space charge limited current (*SCLC*) measurement was conducted to probe the trap density of the electron-only devices (ITO/SnO_2/control and target perovskite/PCBM/Ag). As depicted in Fig. 5e, the trap filling limit voltage (V_{TFL}) of target sample is 0.33 V while the V_{TFL} of control sample is 0.59 V. Subsequently, the trap state density (N_t) can be calculated V_{TFL} through the formula $V_{TFL} = qN_tL^2/(2\varepsilon_r\varepsilon_0)$, where ε_0 is called the vacuum permittivity, ε_r is the relative dielectric constant of perovskite film, q is electron charge and L is the thickness. Then we obtained that the corresponding N_t of different devices are 8.35×10^{15} and 4.67×10^{15} cm^{-3}, respectively, which can manifest the HCOOH passivation effect in target samples and the transport ability improved by ZnO NPs. The dark *J-V* measurements were applied on the corresponding devices, the results shown in Fig. 5f illustrates that the leakage current of target device is obviously lower than that of control device, which indicates that the leakage current is suppressed because of decreased defect density in target device. To further explore the mechanism of enhanced PCE in target device, the relationship between V_{OC} and light intensity (Φ) was provided in Fig. 5g, which can reflect the trap-assisted shockley-reads-hall (SRH) recombination by calculating the slope of the equation $\Delta V_{OC} = nk_BT\Delta\ln\Phi/q$ [37,38]. The n values of control and target devices are 1.79 and 1.23, which indicate that the SRH recombination process is apparently reduced in the target device. These results are consistent with previous experimental results, which is ascribed to the improved crystallinity and the reduction of defects in target film. Moreover, the output stability of devices was also compared in Fig. 5h and i, both PCE and V_{oc} output stabilities of target device are better than that of control device under the test with 20 min every 12 s interval condition due to optimized stability by HCOOH in target device.

Long-term stability remains a critical challenge for PSCs commercialization. However, the introduction of ZnO would improve the photoelectric performance of the devices but also have negative affect on stability because of the deprotonation reaction between MA^+/FA^+ and ZnO in previous reports [39,40]. Deprotonation reaction would change microstructure of the perovskite and cause the film decomposition, thus reducing the stability of the device. But ZnO NPs has no significant impact on the stability of perovskite in this strategy, which could be observed in the long-term stability test results in Fig. S11. Firstly, a small amount of ZnO NPs is introduced to improve the properties of ETL. Meanwhile, appropriate amount of MACl was introduced into the perovskite, which could effectively solve the stability problem result from the deprotonation reaction between perovskite and ZnO. To explain the function of MACl, the interaction energy and weak interactions between $MAPbI_3$-ZnO, $FAPbI_3$-ZnO and MACl-ZnO were analyzed by density functional theory (DFT) in Fig. S12. The Gaussian 09 software package was used for geometric optimization and energy calculation. The PBE0 function combined with D3 (BJ) dispersion correction was used for geometric optimization, where elements C, H, O, and N are based on the 6–31g basis set [41,42]. For the convenience of calculation, Pb, I, and Zn elements were used Los Alamos National Laboratory 2double-ζ(LANL2DZ) pseudo-potential [43–45]. The binding energy (E_{bind}) represents the change in electron energy when two infinitely separated molecules form a complex, calculated as follows: $E_{bind} = E_{AB}$-($E_A + E_B$), where a larger negative value of E_{bind} represents a stronger binding strength [46]. In addition, independent gradient model based on Hirshfeld partition (IGMH) was used to characterize the weak interaction between molecules because it provides a clear visualization of the weak interaction [47].The wave function analysis was performed and visualized using Visual Molecular Dynamics (VMD) software with the help of Multiwfn software package [48,49]. It shows that the E_{bind} of $FAPbI_3$-ZnO, $MAPbI_3$-ZnO and MACl-ZnO are −7.04 kcal mol^{-1}, -6.72 kcal mol^{-1} and -9.31 kcal mol^{-1}, respectively, indicating that the binding strength of MACl and ZnO is the highest [46]. Furthermore, IGMH analysis shows that weak van der Waals interactions exist between $FAPbI_3$-ZnO and $MAPbI_3$-ZnO, and a stronger intermolecular force exists between MACl and ZnO because of the darker color of the iso-surfaces [50]. The highest interaction between MACl and ZnO indicates that the ZnO would interact with MA^+ of MACl rather than MA^+/FA^+ in perovskite material, which protects the microstructure of photoactive layer. The long-term stability tests of target devices with/-without modifying by MACl were displayed in Fig. S13, which illustrate that MACl could protect film from the deprotonation reaction. Subsequently, the XRD measurements of fresh film and after exposing 100 days were displayed in Fig. S14, which illustrate the high stability of target film. Finally, the long-term test results of the control and target devices under different conditions were demonstrated in Fig. 6. Fig. 6a exhibits the test results of an unencapsulated target device under the air atmosphere with temperature ~25 °C and relative humidity ~20 % conditions for 3000 h, which shows that the target device can still maintain more than 83 % of the initial PCE while an unencapsulated control device can only maintain 30 % of the initial PCE, which illustrates that the target device has high stability because of the optimization of the HCOOH vapor annealing method. Furthermore, Fig. 6b illustrates that target device could maintain more than 85 % of initial PCE under continuous illumination, while the control device would decay to 48 % of initial PCE. The similar trend is also shown in the test of high humidity (~80 %) stability test in Fig. 6c, which indicate that the target device could maintain about 86 % of initial PCE whereas only 38 % for control device.

3. Conclusion

In this study, we report a synchronous optimization strategy by HCOOH vapor annealing process and SnO_2: ZnO NPs composite ETL. The HCOOH vapor annealing method provides a appropriate physical and chemical environment for perovskite growth ($(FAPbI_3)_{0.9}$-$MAPbBr_3)_{0.1}$), which realizes improved crystallinity with larger grain size in perovskite film and optimizes the transport properties of ETL. The optimized perovskite film exhibits excellent photoelectric properties and fewer defects due to the passivation effect of HCOOH. Simultaneously, MACl in perovskite can inhibit the deprotonation reaction caused by introduction of ZnO NPs, which was also verified by DFT calculations. Finally, the PSCs fabricated by this synchronous optimization strategy achieved a PCE of 23.41 % with an improved V_{OC} of 1.19 V, a J_{SC} of 24.38 mA cm^{-2} and *FF* of 80.70 %with outstanding stability under different conditions of long-term stability.

4. Experimental section

Materials: SnO_2 aqueous colloidal dispersion (15 wt%) was purchased from Alfa Aesar. HCOOH was purchased from Aladdin. Lead diiodide (PbI_2) and lead dibromide ($PbBr_2$) were purchased from Tokyo Chemical Industry Co., Ltd. Formamidine iodide (FAI), methylammonium bromide (MABr) and methylammonium chloride (MACl) were purchased from GreatCell Solar. N, N-dimethylformamide (DMF, 99.8 %, anhydrous), dimethylsulfoxide (DMSO, 99.8 %, anhydrous) and chlorobenzene (CB,99.8 %, anhydrous) ZnO nanoparticle ink was purchased from Sigma-Aldrich. Isopropyl alcohol (IPA) was purchased Sinopharm Chemical Reagent Co., Ltd. All materials were used directly without further purification.

$(FAPbI_3)_{0.9}(MAPbBr_3)_{0.1}$ precursor solution preparation: The precursor solution was mixed by $FAPbI_3$ and $MAPbBr_3$ solution with v/v of 9:1, which was composed of FAI (185.7 mg), PbI_2 (522.8 mg), MABr (13.4 mg), $PbBr_2$ (46.2 mg) and MACl (20 mg) in solvent (DMF: DMSO with v/v of 4:1).

Composite ETL solution preparation: SnO_2 colloidal dispersion was

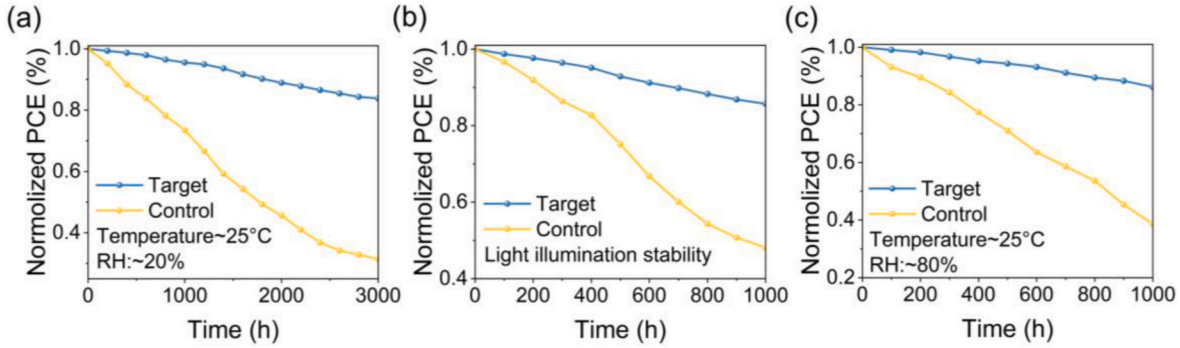

Fig. 6. Long-term stability performance of three devices a) in ~25 °C and ~20 % RH under air atmosphere b) light illumination and c) moisture atmosphere.

diluted with 5 wt% water and the ZnO NPs ink dissolved in IPA with v/v of 1:10.

Spiro-OMeTAD solution preparation: The solution was composited by 72.3 mg spiro-OMeTAD, 17.5 μL Li-TFSI and 28.8 μL tBP solution (520 mg Li-TFSI was dissolved in 1 mL acetonitrile) dissolved in CB (1 mL).

Device fabrication: ITO glass substrates (0.7 mm thick, 1.7 cm × 1.7 cm, $R_s \leq 10\Omega$ sq^{-1}) were washed in an ultrasonic bath of deionized water, acetone, IPA, ethanol for 20 min then drying in the oven. The substrates were exposed to ultraviolet ozone (UVO) for 20 min to clean substrates and enhance the hydrophobicity. After cooling to room temperature, SnO_2 colloidal dispersion was coated on the ITO substrate in air at 5000 rpm for 30 s, then annealed at 160 °C for 10 min and treated with UVO for 20 min. ZnO NPs were coated on the SnO_2 in air at 5000 rpm for 30 s, then annealed at 100 °C for 10 min. After treating with UVO for 20 min to clean the film and enhance the hydrophobicity, the precursor solution was spin coated on the composite ETL layer. Then the film was put into the sealed container with pre-heated HCOOH vapor and put them into oven with 100 °C to anneal the film for 15 min. The spiro-OMeTAD solution was spin-coated at 4000 rpm for 30 s. Finally, Ag electrode with 120 nm thickness was thermally evaporated through a 0.052 cm^2 mask on the device under $<5 \times 10^{-4}$ Pa vacuum condition.

Characterizations: The AFM and KPFM results were tested using the MFP-3D (Oxford Instruments, USA) equipment from the Instrumental Analysis Center of Shanghai Jiao Tong University. The SEM images were obtained using Gemini SEM300. FLS1000 (Edinburgh Instruments, UK) with the excitation wavelength of 405 nm and frequency of 20 MHz was used to test the steady-state PL and TRPL spectra. TOF-SIMS was performed by ION-TOF GmbH/TOF-SIMS 5–100 system with an analysis area of 100 × 100 μm^2. The crystal structures of films were obtained by XRD (Bruker, D8 ADVANCE Da Vinci) using a Cu Kα ($\lambda = 0.15406$ nm) source. The UV–vis absorption spectra were obtained with a UV–vis–NIR spectrophotometer (PerkinElmer, Lamda 950). FTIR measurements were conducted on a Thermo Fisher/Nicolet 6700 instrument. EQE measurements were performed on a quantum efficiency/IPCE system (PV Measurements Inc., QEX10) in the 300–850 nm wavelength range. The photocurrent density-voltage (*J-V*) curves of the PSCs were tested in an N_2-filled glovebox using a programmable Keithley 2400 source meter and a 300 W class AAA solar simulator (ENLITECH, SS-X50). The intensity of solar simulator was calibrated to AM1.5G (100 mW cm^{-2}) with a filtered KG1 (ENLITECH, SRC2020) silicon reference solar cell.

Operational stability test of PSCs: The long-term stability of the PSCs was evaluated under three distinct conditions: ambient stability, humidity stability, and light stability. Unencapsulated devices were stored in an ambient air environment (approximately 25 °C and 20 % relative humidity) for 3000 h to assess ambient stability. For humidity stability testing, the devices were exposed to a controlled air environment with 80 % relative humidity at 25 °C. Light stability was characterized by subjecting the devices to continuous AM 1.5G illumination inside a nitrogen-filled glovebox.

CRediT authorship contribution statement

Haotian Zhang: Conceptualization. **Chao Gao:** Conceptualization. **Li He:** Formal analysis. **Dezhao Zhang:** Investigation. **Hongzhen Su:** Methodology. **Hong Liu:** Resources. **Kadi Zhu:** Supervision. **Wenzhong Shen:** Supervision, Funding acquisition.

Declaration of competing interest

The authors declare the following financial interests/personal relationships which may be considered as potential competing interests: Wenzhong Shen reports financial support was provided by Shanghai Jiao Tong University. Wenzhong Shen reports a relationship with Shanghai Jiao Tong University that includes: funding grants. If there are other authors, they declare that they have no known competing financial interests or personal relationships that could have appeared to influence the work reported in this paper.

Acknowledgements

The work in this dissertation has been fully supported by the National Natural Science Foundation of China (Grant No. 11834011) and the Shanghai New Energy Technology Research and Development Project (Grant No. 24DZ3000900).

Appendix A. Supplementary data

Supplementary data to this article can be found online at https://doi.org/10.1016/j.solmat.2025.113821.

Data availability

Data will be made available on request.

References

[1] F.P. García de Arquer, A. Armin, P. Meredith, E.H. Sargent, Solution-processed semiconductors for next-generation photodetectors, Nat. Rev. Mater. 2 (2017) 16100.
[2] V. D'Innocenzo, G. Grancini, M.J.P. Alcocer, A.R.S. Kandada, S.D. Stranks, M. M. Lee, G. Lanzani, H.J. Snaith, A. Petrozza, Excitons versus free charges in organo-lead tri-halide perovskites, Nat. Commun. 5 (2014) 3586.
[3] Q. Lin, A. Armin, R.C.R. Nagiri, P.L. Burn, P. Meredith, Electro-optics of perovskite solar cells, Nat. Photonics 9 (2015) 106–112.
[4] W. Abu Labana, L. Etgar, Depleted hole conductor-free lead halide iodide heterojunction solar cells, Energy Environ. Sci. 6 (2013) 3249–3253.
[5] G. Xing, N. Mathews, S. Sun, S.S. Lim, Y.M. Lam, M. Grätzel, S. Mhaisalkar, T. C. Sum, Long-range balanced electron- and hole-transport lengths in organic-inorganic $CH_3NH_3PbI_3$, Science 342 (2013) 344–347.
[6] I. Raifuku, Y. Ishikawa, S. Ito, Y. Uraoka, Characteristics of perovskite solar cells under low-illuminance conditions, J. Phys. Chem. C 120 (2016) 18986–18990.
[7] J. Lin, M. Lai, L. Dou, C.S. Kley, H. Chen, F. Peng, J. Sun, D. Lu, S.A. Hawks, C. Xie, F. Cui, A.P. Alivisatos, D.T. Limmer, P. Yang, Thermochromic halide perovskite solar cells, Nat. Mater. 17 (2018) 261–267.

[8] H. Wu, Y. Cheng, J. Ma, J. Zhang, Y. Zhang, Y. Song, S. Peng, Pivotal routes for maximizing semitransparent perovskite solar cell performance: photon propagation management and carrier kinetics regulation, Adv. Mater. 35 (2023) 2206574.

[9] T. Moot, J.B. Patel, G. McAndrews, E.J. Wolf, D. Morales, I.E. Gould, B.A. Rosales, C.C. Boyd, L.M. Wheeler, P.A. Parilla, S.W. Johnston, L.T. Schelhas, M.D. McGehee, J.M. Luther, Temperature coefficients of perovskite photovoltaics for energy yield calculations, ACS Energy Lett. 6 (2021) 2038–2047.

[10] J. Du, J. Chen, B. Ouyang, A. Sun, C. Tian, R. Zhuang, C. Chen, S. Liu, Q. Chen, Z. Li, X. Wu, J. Cai, Y. Zhao, R. Li, T. Xue, T. Cen, K. Zhao, C. Chen, Face-on oriented self-assembled molecules with enhanced π–π stacking for highly efficient inverted perovskite solar cells on rough FTO substrates, Energy Environ. Sci. 18 (2015) 3196–3210.

[11] W. Shockley, H.J. Queisser, Detailed balance limit of efficiency of p-n junction solar cells, J. Appl. Phys. 32 (1961) 510–519.

[12] G.E. Eperon, V.M. Burlakov, P. Docampo, A. Goriely, H.J. Snaith, Morphological control for high performance, solution-processed planar heterojunction perovskite solar cells, Adv. Funct. Mater. 24 (2014) 151–157.

[13] A. Dualeh, N. Tétreault, T. Moehl, P. Gao, M.K. Nazeeruddin, M. Grätzel, Effect of annealing temperature on film morphology of organic-inorganic hybrid pervoskite solid-state solar cells, Adv. Funct. Mater. 24 (2014) 3250–3258.

[14] Y. Deng, Z. Ni, A.F. Palmstrom, J. Zhao, S. Xu, C.H. Van Brackle, X. Xiao, K. Zhu, J. Huang, Y. Deng, Z. Ni, A.F. Palmstrom, J. Zhao, S. Xu, C.H. Van Brackle, X. Xiao, K. Zhu, J. Huang, Reduced self-doping of perovskites induced by short annealing for efficient solar modules, Joule 4 (2020) (2020) 1949–1960.

[15] M. Kim, G.-H. Kim, K.S. Oh, Y. Jo, H. Yoon, K.-H. Kim, H. Lee, J.Y. Kim, D.S. Kim, High-temperature–short-time annealing process for high-performance large-area perovskite solar cells, ACS Nano 11 (2017) 6057–6064.

[16] Q. Zhou, Z. Jin, H. Li, J. Wang, Enhancing performance and uniformity of $CH_3NH_3PbI_{3-x}Cl_x$ perovskite solar cells by air-heated-oven assisted annealing under various humidities, Sci. Rep. 6 (2016) 21257.

[17] N. Li, X. Niu, L. Li, H. Wang, Z. Huang, Y. Zhang, Y. Chen, X. Zhang, C. Zhu, H. Zai, Y. Bai, S. Ma, H. Liu, X. Liu, Z. Guo, G. Liu, R. Fan, H. Chen, J. Wang, Y. Lun, X. Wang, J. Hong, H. Xie, D.S. Jakob, X.G. Xu, Q. Chen, H. Zhou, Liquid medium annealing for fabricating durable perovskite solar cells with improved reproducibility, Science 373 (2021) 561–567.

[18] J. Chen, J. Du, J. Cai, B. Ouyang, Z. Li, X. Wu, C. Tian, A. Sun, R. Zhuang, X. Wu, C. Chen, T. Cen, R. Li, T. Xue, Y. Zhao, K. Zhao, Q. Chen, C.-C. Chen, Lewis base strategy for crystallization control and buried interface passivation on hydrophobic PTAA substrate for efficient tin–lead perovskite and all-perovskite tandem solar cells, ACS Energy Lett. 10 (2025) 1117–1128.

[19] X. Huang, G. Deng, S. Zhan, F. Cao, F. Cheng, J. Yin, J. Li, B. Wu, N. Zheng, Solvent gaming chemistry to control the quality of halide perovskite thin films for photovoltaics, ACS Cent. Sci. 8 (2022) 1008–1016.

[20] C.-M. Hsieh, Y.-S. Liao, Y.-R. Lin, C.-P. Chen, C.-M. Tsai, E. Wei-Guang Diau, S.-C. Chuang, Low-temperature, simple and efficient preparation of perovskite solar cells using lewis bases urea and thiourea as additives: stimulating large grain growth and providing a PCE up to 18.8%, RSC Adv. 8 (2018) 19610.

[21] X. Jiao, W.-M. Gu, Y. Xu, K.-J. Jiang, G. Yu, Q.-W. Zhang, C.-Y. Gao, C.-M. Liu, X.-H. Fan, L.-M. Yang, Y. Song, Anion-exchange assisted sequential deposition for stable and efficient $FAPbI_3$-based perovskite solar cells, Chem. Eng. J. 452 (2023) 139326.

[22] W.-M. Gu, K.-J. Jiang, X. Jiao, L. Wu, C.-Y. Gao, X.-H. Fan, L.-M. Yang, Q. Wang, Y. Song, Poly(3,4-Ethylenedioxythiophene) as a hole-transport layer for highly efficient and stable inverted perovskite solar cells, Chem. Eng. J. 485 (2024) 149512.

[23] T. Xia, Q. Li, Z. Xue, Y. Miao, X. Shen, X. Zhao, Boosting the structural and electrochemical stability of chloride-ion-conducting perovskite solid electrolytes by alkali ion doping, Adv. Mater. 37 (2025) 2411605.

[24] L. Wang, G. Liu, X. Xi, G. Yang, L. Hu, B. Zhu, Y. He, Y. Liu, H. Qian, S. Zhang, H. Zai, Annealing engineering in the growth of perovskite grains, Crystals 12 (2022) 894.

[25] J. You, Y. Yang, Z. Hong, T.-B. Song, L. Meng, Y. Liu, C. Jiang, H. Zhou, W.-H. Chang, G. Li, Y. Yang, Moisture assisted perovskite film growth for high performance solar cells, Appl. Phys. Lett. 105 (2014) 183902.

[26] J. Huang, X. Yu, J. Xie, D. Xu, Z. Tang, C. Cui, D. Yang, Ambient engineering for high-performance organic-inorganic perovskite hybrid solar cells, ACS Appl. Mater. Inter. 8 (2016) 21505–21511.

[27] X. Wang, H. Wang, T. Shan, Q. Ma, Y. Chen, L. Chen, X. Zhao, F. Wang, Fluorocarbon-based solvent-bath annealing for high-performance perovskite photovoltaics, Adv. Funct. Mater. 35 (2025) 2413400.

[28] J. Liu, C. Gao, X. He, Q. Ye, L. Ouyang, D. Zhuang, C. Liao, J. Mei, W. Lau, Improved crystallization of perovskite films by optimized solvent annealing for high efficiency solar cell, ACS Appl. Mater. Interfaces 7 (2015) 24008–24015.

[29] L. He, H. Su, Z. Li, H. Liu, W. Shen, Multiple function synchronous optimization by PbS quantum dots for highly stable planar perovskite solar cells with efficiency exceeding 23%, Adv. Funct. Mater. 33 (2023) 2213963.

[30] Y. Zhang, M. Yang, J. Du, L. Yang, L. Fan, X. Liu, J. Yang, F. Wang, Modulation of Ni^{3+} and crystallization of dopant-free NiO_x hole transporting layer for efficient p-i-n perovskite solar cells, Electrochim. Acta 319 (2019) 41–48.

[31] D. Zhou, D. Liu, G. Pan, X. Chen, D. Li, W. Xu, X. Bai, H. Song, A novel and efficient downconverter for improving the performance of silicon solar cells, Adv. Mater. 29 (2017) 1704149.

[32] D. Bi, C. Yi, J. Luo, J. Décoppet, F. Zhang, S.M. Zakeeruddin, X. Li, A. Hagfeldt, M. Grätzel, Polymer-templated nucleation and crystal growth of perovskite films for solar cells with efficiency greater than 21%, Nat. Energy 1 (2016) 16142.

[33] S. Chen, X. Xiao, B. Chen, L.L. Kelly, J. Zhao, Y. Lin, M.F. Toney, J. Huang, Crystallization in one-step solution deposition of perovskite films: upward or downward, Sci. Adv. 7 (2021) eabb2412.

[34] J.-W. Lee, S.-H. Bae, N.-D. Marco, Y.-T. Hsieh, Z. Dai, Y. Yang, The role of grain boundaries in perovskite solar cells, mater, Today Energy 7 (2017) 149–160.

[35] Z. Li, R. Wang, J. Xue, X. Xing, C. Yu, T. Huang, J. Chu, K.-L. Wang, C. Dong, Z. Wei, Y. Zhao, Z.-K. Wang, Y. Yang, Core–shell $ZnO@SnO_2$ nanoparticles for efficient inorganic perovskite solar cells, J. Am. Chem. Soc. 141 (2019) 17610–17616.

[36] R. Li, G. Zhang, Y. Wang, Z. Lin, C. He, Y. Li, X. Ren, P. Zhang, H. Mi, Fast ion diffusion kinetics based on ferroelectric and piezoelectric effect of $SnO_2/BaTiO_3$ heterostructures for high-rate sodium storage, Nano Energy 90 (2021) 106591.

[37] J. Wang, R. Zhang, H. Xu, Y. Chen, H. Zhang, N.-G. Park, Polyacrylic acid grafted carbon nanotubes for immobilization of lead (II) in perovskite solar cell, ACS Energy Lett. 7 (2022) 1577–1585.

[38] H. Zhang, K. Li, M. Sun, F. Wang, H. Wang, A.K.-Y. Jen, Design of superhydrophobic surfaces for stable perovskite solar cells with reducing lead leakage, Adv. Energy Mater. 11 (2021) 2102281.

[39] S. Apergi, G. Brocks, S. Tao, S. Olthof, Probing the reactivity of ZnO with perovskite precursors, ACS Appl. Mater. Interfaces 16 (2024) 14984–14994.

[40] G. Liu, Y. Zhong, H. Mao, J. Yang, R. Dai, X. Hu, Z. Xing, W. Sheng, L. Tan, Y. Chen, Highly efficient and stable ZnO-based MA-free perovskite solar cells via overcoming interfacial mismatch and deprotonation reaction, Chem. Eng. J. 431 (2022) 134235.

[41] V. Vetere, C. Adamo, P. Maldivi, Performance of the 'parameter free' PBE0 functional for the modeling of molecular properties of heavy metals, Chem. Phys. Lett. 325 (2000) 99–105.

[42] S. Grimme, J. Antony, S. Ehrlich, H. Krieg, A consistent and accurate ab initio parametrization of density functional dispersion correction (DFT-D) for the 94 elements H-Pu, J. Chem. Phys. 132 (2010) 154104.

[43] Y. Yang, M.N. Weaver, K.M. Merz Jr., Assessment of the "6-31+G** + LANL2DZ" mixed basis set coupled with density functional theory methods and the effective core potential: prediction of heats of formation and ionization potentials for first-row-transition-metal complexes, J. Phys. Chem. A 113 (2009) 9843–9851.

[44] X. Song, W. Dong, X. Hou, Q. Zhao, Z. Zhang, Y. Ren, The high fluorescence sensitivity property and quenching mechanism of one-dimensional Cd-HCIA-1 sensor for nitrobenzene, Phys. Chem. Chem. Phys. 25 (2023) 14907–14917.

[45] H. Kruse, L. Goerigk, S. Grimme, Why the standard B3LYP/6-31G* model chemistry should not be used in DFT calculations of molecular thermochemistry: understanding and correcting the problem, J. Org. Chem. 77 (2012) 10824–10834.

[46] Z. Liu, X. Wang, T. Lu, A. Yuan, X. Yan, Potential optical molecular switch: lithium@cyclo[18]carbon complex transforming between two stable configurations, Carbon 187 (2022) 78–85.

[47] T. Lu, Q. Chen, Independent gradient model based on hirshfeld partition: a new method for visual study of interactions in chemical systems, J. Comput. Chem. 43 (2022) 539–555.

[48] T. Lu, F. Chen, Multiwfn: a multifunctional wavefunction analyzer, J. Comput. Chem. 33 (2012) 580–592.

[49] W. Humphrey, A. Dalke, K. Schulten, VMD: visual molecular dynamics, J. Mol. Graph. 14 (1996) 33–38.

[50] X. Song, Q. Zhao, M. Dang, X. Hou, S. Liu, Z. Ma, Y. Ren, Quenching and enhancement mechanisms of a novel Cd-based coordination polymer as a multiresponsive fluorescent sensor for nitrobenzene and aniline, Anal. Chim. Acta 1316 (2024) 342865.